Zero-bias conductance peak in tunneling spectroscopy of hybrid superconductor junctions

Shin-Tza Wu[1] and Chung-Yu Mou[1,2,*]
[1]*Department of Physics, National Tsing Hua University, Hsinchu 30043, Taiwan*
[2]*National Center for Theoretical Sciences, P.O. Box 2-131, Hsinchu, Taiwan*
(Received 30 May 2002; revised manuscript received 9 September 2002; published 13 January 2003)

A generalized method of image, incorporated with the nonequilibrium Keldysh-Green's function formalism, is employed to investigate the tunneling spectroscopy of hybrid systems in the configuration of planar junction. In particular, tunneling spectroscopies of several hybrid systems that exhibit zero-bias conductance peaks (ZBCP's) are examined. The well-known metal–*d*-wave superconductor (ND) junction is examined in detail. Both the evolution of the ZBCP versus doping and the splitting of the ZBCP in magnetic fields are computed in the framework of the slave-boson mean field theory. Further extension of our method to analyze other states shows that states with particle-hole pairing, such as *d*-density wave and graphene sheet, are all equivalent to a simple one-dimensional model, which at the same time also describes the polyacetylene. We provide the criteria for the emergence of ZBCP. In particular, broken reflection symmetry at the microscopic level is shown to be a necessary condition for ZBCP to occur.

DOI: 10.1103/PhysRevB.67.024503 PACS number(s): 74.20.Mn, 74.50.+r, 74.45.+c

I. INTRODUCTION

Since the pioneering work of Giaever,[1] the tunneling measurement has been a major experimental method for investigations into the electronic states of condensed matter systems.[2] In the simplest setup, a metal with *known* spectral property is made in contact with a material *X*, forming an *NX* junction so that the electronic states of *X* can be probed. For many years, despite the fact that many insights into the spectral properties of many states have been gained from the differential conductance (dI/dV) curves obtained from tunneling measurements, nonetheless, unlike many other experiments, it is fair to say that there is no clear and solid statement as to exactly what bulk properties are being probed in tunneling measurements. For example, it is known that in neutron scattering experiments, the neutron intensity is a measure of the imaginary part of the bulk spin susceptibility, $\mathrm{Im}\,\chi(\mathbf{k},\omega)$; no similar statement has ever been firmly established for tunneling measurements.

The difficulty for establishing the relation between the tunneling conductance and the bulk quantities can be traced back to the very existence of the junction interface. It has been realized that the presence of the interface can change the conductance curve dramatically. A well-known example is the zero-bias conductance peak (ZBCP) observed in the tunneling spectra when *X* is a *d*-wave superconductor (ND junction) in (110) direction.[3] The appearance of the ZBCP is entirely tied up with the presence of the interface and its orientations, and therefore can not be obtained by simple calculations based on bulk density of states.

Recent theoretical analyses of the ZBCP have been mostly concentrated on the ND junctions. Furthermore, they are based largely on the standard BTK theory.[4] In the continuum limit, analytic expressions of the differential conductance for general orientations of the interface were obtained. Numerical calculations were later carried out for the BTK theory in the lattice version.[5–7] While these works have supplied insights into the ZBCP, they are, however, specifically designed for studying the ND junction. Moreover, because the relation of the conductance curve to the bulk quantities was not clearly manifested, essentially the numerical computation had to be done individually for each interface orientation. Another technical inconvenience is that the BTK theory is a mean-field theory based on solving the mean-field quasiparticle wave functions, it is thus difficult in this formulation to take into account the effects of interaction systematically. To extend into the study of other systems, especially those with strong correlations where almost all relevant models are on discrete lattices, it is therefore an urgent need to have a formulation which can go beyond the mean-field BTK formulation. As an illustration of our approach, in this paper we will focus on mean-field analysis of several tunneling problems. The effects of fluctuations and interactions will be discussed elsewhere.

In this paper, we shall adopt an approach that is based on the non-equilibrium Keldysh-Green's function formalism. In the lowest order approximation, we are able to express the differential conductance entirely in terms of bulk Green's functions and include the interface effects. Thus, the relation of the conductance curve to the bulk quantities is clearly manifested. The tunneling between *N* and *X* will be treated as a perturbation, so that in the zeroth order the Green's function is the mean-field *half-space* Green's function that resides only on the semi-infinite plane and satisfies the boundary conditions to be specified later. Based on the half-space Green's function *g*, higher order corrections can be systematically constructed.[7–9] In particular, a class of infinite series in *g*, which consists of all elastic tunneling processes in the perturbation theory, will be considered and summed to all orders for calculating the current across the junction.[7,10,11] To fully take into account the tight-binding nature of the problem, we shall employ discrete models for both the materials *N* and *X* and the tunnel junctions. Thus the essential quantity to be calculated is the half-space lattice Green's function for the *X* state. In resemblance to the conventional method of image, we express the half-space Green's function in terms of the bulk Green's functions propagating from the real source and a fictitious image source

$$g = G_{\text{real}} - G_{\text{imag}} \times \alpha \tag{1}$$

with the factor α accounting for the boundary conditions. The half-space Green's function is thus decomposed into two parts: the real-source part comes solely from the bulk and hence reveals purely the bulk properties, the image part contains all interface effects which are encoded in the factor α. In this way, the interface effects are clearly identified in the course of the analysis and one can pinpoint any departure from the bulk property.

The factor α can be expressed in terms of bulk Green's function. Right on the interface, it is found

$$\alpha_0 = G^{-1}(d)G(-d). \tag{2}$$

Here d is an effective lattice constant whose precise meaning will be explained in below. Clearly, the tunneling spectrum can be classified according to whether the reflection symmetry is broken or not. In the case when reflection symmetry is broken with respect to the interface, one has $G(-d) \neq G(d)$, hence α_0 is not unity, possible zero modes may arise due to the presence of zeros in the denominator of the left hand side. The number of localized zero modes is thus determined by the order of zeros in the bulk Green's function $G(d)$. In the lowest order approximation, the differential conductance is given by the local density of states at the interface

$$dI/dV \propto -\sum_{\mathbf{k}\sigma} \text{Im}\{g_0(\mathbf{k}, eV)\}, \tag{3}$$

where g_0 is g of Eq. (1) evaluated at the interface and e is the charge of an electron. Since α_0 can be expressed entirely in terms of bulk Green's functions, this is then the relation between the bulk quantities and the differential conductance alluded to earlier.

This paper is organized as follows. In Sec. II, we outline the theoretical formulation and derive the generalized method of image for discrete lattices. In Sec. III this method is applied to the study of tunneling spectroscopies for various systems. We first study the ND junctions at various surface orientations and examine the doping dependence of the ZBCP using mean-field slave boson theory. We then study the effects of applied magnetic fields perpendicular to the *ab* plane. A one-dimensional (1D) model, based on the structure of polyacetylene, is then studied in Sec. III C. On the basis of this model, we further apply this method to investigate tunneling into *d*-density-wave states and graphite sheets. We conclude in Sec. IV with some comments on the significance and further applications of our formulation. The Appendix describes techniques for deriving the current expressions for the tunnel junctions studied in the text.

II. THEORETICAL FORMULATION AND GENERALIZED METHOD OF IMAGE

A. Theoretical model

We start by modeling the planar junction. As illustrated in Fig. 1, the tunnel junction consists of two truncated two-dimensional lattices connected through a tunnel barrier, with

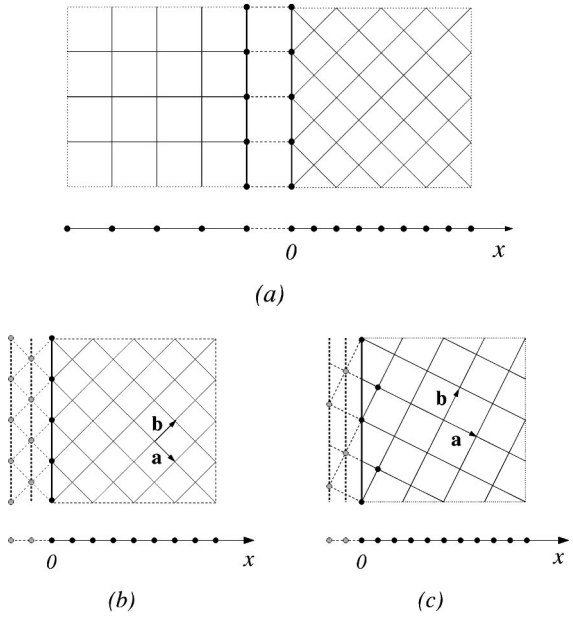

FIG. 1. (a) A typical configuration for the tunnel junctions studied in this paper: a (100) lattice on the left side connected to a (110) lattice on the right side. The dashed lines between the two lattices indicate hopping due to the tunneling Hamiltonian H_T. The effective one dimensional lattices obtained from Fourier transformation along the direction parallel to the interface are shown in below. In (b) and (c) we show explicitly the hard walls of semi-infinite lattices at (110) and (210) orientations indicated by open circles. Here a and b indicate the crystalline axes. The hard walls result from disconnecting the sample from the left side in the zeroth order of H_T. Note that third hard wall would be needed if one considers n.n.n. hopping in the (210) orientation.

the left half the normal (N) electrode ($-\infty < x \leqslant -a_L$, a_L is the lattice constant) and the right the test (X) electrode ($0 \leqslant x < \infty$).[12] We take the interface the y direction. The total Hamiltonian of the system thus comprises two parts: the Hamiltonian $H_0 = H_L + H_R$ for the left and right electrodes, and the tunneling Hamiltonian which connects the surface points at $x = -a_L$ and $x = 0$

$$H_T = \sum_{y_l, y_r, \sigma} t_I(|y_l - y_r|) c^\dagger_{l\sigma} c_{r\sigma} + \text{H.c.} \tag{4}$$

Here σ are spin indices, and y_l, y_r are the y coordinates of the surface sites on the left and right electrodes; $c_{l\sigma}$, $c_{r\sigma}$ are the corresponding electron annihilation operators. t_I is the tunneling amplitude whose magnitude models the barrier height in the tunnel junction. Since all points over the interface layers contribute to the tunneling process, one has to sum over all interface sites. Suppose the chemical potentials on the left and the right electrodes are μ_L and μ_R, respectively, the total grand Hamiltonian is then given by

$$K = (H_L - \mu_L N_L) + (H_R - \mu_R N_R) + H_T \equiv K_0 + H_T, \tag{5}$$

where $(\mu_L - \mu_R)$ is fixed to be the voltage drop eV.

To calculate the tunneling current, we choose the unperturbed state to be the ground state of K_0 and adiabatically

turn on H_T. In the Heisenberg picture, the tunneling current is then found to be[13] (we set $\hbar=1$ throughout)

$$I(t)=+ie\sum_{y_l,y_r,\sigma}\{t_I\langle c^\dagger_{l\sigma}c_{r\sigma}\rangle-t_I^*\langle c^\dagger_{r\sigma}c_{l\sigma}\rangle\}. \tag{6}$$

The expectation values $\langle\cdots\rangle$ here represent the ensemble average $\mathrm{Tr}[Z^{-1}\exp(-\beta K_0)\cdots]$.

In actual experiments, the normal metal on the left electrode could be in any orientations, and the detail connection between the two lattices may also cause complications in the tunneling spectroscopy. To be definite, however, in our model we fix the lattice on the left side at (100) orientation and connect its boundary sites to those of the right at $x=0$ [Fig. 1(a)]. As one can observe easily, the system is translational invariant along the interface direction with period a_L. We exploit this symmetry by making a partial Fourier transformation along the interface direction in Eq. (6) and arriving at

$$I(t)=+ie\sum_{k_y,\sigma}t_I(k_y)\langle c^\dagger_{l\sigma}(k_y)c_{r\sigma}(k_y)\rangle+\mathrm{H.c.}, \tag{7}$$

where $-\pi/a_L<k_y\leqslant\pi/a_L$. We emphasize that the problem is now effectively one dimensional: in Eq. (7) different k_y modes are decoupled completely. Moreover, only *Surface* quantities are involved. These are very appealing features especially for the feasibility of our method of image, as we will discuss in the following section.

In the Keldysh Green's function formulation, the time evolution of the density matrix can be formally solved as a closed time-ordered path integral.[14] The expectation value $\langle c^\dagger_{l\sigma}(k_y)c_{r\sigma}(k_y)\rangle$ in Eq. (7) is then related to the components of Keldysh's Green's functions over the closed time path. One can then calculate perturbatively the average current I in terms of the zeroth order Green's function. Details of this calculation can be found in Ref. 7 and an outline is presented in the Appendix. Here an essential difference from earlier work is that previously the Green's functions were obtained through directly solving the equation of motion, while here we shall make use of the method of image elucidated in the following section. In this way the current approach is more general and versatile, and can be easily applied to various hybrid systems.

B. Generalized method of image

In the Green's function approach, the building blocks for calculating the current are the zeroth order half-space Green's functions (see the Appendix). Because in the zeroth order, lattices on the left and right sides are disconnected, the Green's functions are defined only for each semi-infinite plane. Therefore, lattice points on the interface have ''dangling bonds'' which effectively, as shown in Figs. 1(b) and 1(c), impose hard-wall boundary conditions at the end points. One thus envisages a method of image similar to that in electrostatics.

In the usual practice, the method of image is done for the continuum differential equations. It is based on the principle of superposition and the uniqueness of the solutions.[15] When applying it to the discrete lattice, one encounters the difficulty that the image point to any source point **r**, may not locate right at the allowed lattice points. This can be overcome by performing Fourier transformation along the surface direction, chosen as the y direction. In the following sections, we shall further assume that each electrode is in a steady state and thus will be concerned with the half-space Green's function in its Fourier space representation $g(x,x';k_y;\omega)$. For each k_y and ω one is therefore dealing with an effective 1D system (Fig. 1).

As a demonstration of the method, let us consider a 2D semi-infinite square lattice with lattice constant a extending over the region $x\geqslant 0$ at orientation $(hk0)$. The hard-wall boundary condition prescribes the half-space Green's functions to vanish over the hard walls, which consist of all points where the boundary sites can reach away from the bulk lattice [Figs. 1(b), 1(c)]. For general surface orientations $(hk0)$ and with only nearest-neighbor (NN) hopping one can find that the number of hard walls is given by $\max\{|h|,|k|\}$. Let us consider first the single hard-wall configurations, which includes the (100) and the (110) orientations (when there is no next NN hopping in the latter). As we shall discuss later, the multi-hard-wall problem are simple generalizations to the single hard-wall cases.

For single hard-wall case, since there is only one hard wall located at $x=-d$ with $d=a/\sqrt{h^2+k^2}$ being the spacing between two consecutive $(hk0)$ planes, one imposes the boundary condition

$$g(-d,x';k_y;\omega)=0. \tag{8}$$

To implement the method of image, we construct the half-space Green's function $g(x,x';k_y;\omega)$ from the full-space Green's function $G(x,x';k_y;\omega)$ as

$$g(x,x';k_y;\omega)=G(x,x';k_y;\omega)-G(x,x_1';k_y;\omega)\alpha(x';k_y;\omega), \tag{9}$$

where $x_1'=-2d-x'$ is the image point of the point source x' with respect to the hard wall $x=-d$. The Green's function $G(x,x')$ describes direct propagation from the point source to the point x, while $G(x,x_1')$ propagates from the image point to x. The factor α is determined by fitting the boundary condition (8), which yields

$$\alpha(x')=G^{-1}(-d,-2d-x')G(-d,x')=G^{-1}(d+x')G(-d-x'). \tag{10}$$

Here and in the following we suppress the k_y and ω dependence whenever no confusion would arise. In going from the first to the second expressions above, we have used $G(x,x')=G(x-x')$, namely that the full-space Green's functions are translational invariant along the x direction. However, this is not essential for establishing the method of image. It is used here only for brevity. For systems without translational symmetry along x direction, the following discussion still proceeds with only minor modification.

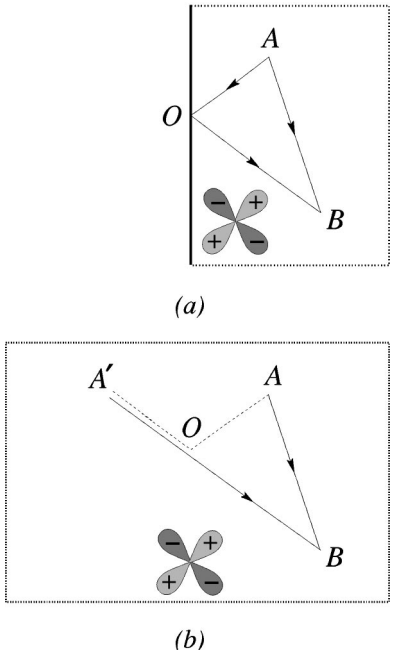

FIG. 2. The method of image applied to *d*-wave superconductors: the propagation (a) from the source A to the point B through the reflected path AOB in the presence of a hard-wall boundary can be replaced by (b) a direct path $A'B$ emanating from a fictitious source at A' where the boundary is absent.

From the half-space Green's function $g(x,x')$, one obtains the surface Green's function g_0 by setting $x=x'=0$. In the Fourier space, g_0 can be expressed by

$$g_0=\sum_{-\pi/d\leqslant k_x<\pi/d} G(k_x)\times[1-\exp(2ik_xd)\alpha_0]. \quad (11)$$

Here $\alpha_0=\alpha(0)$ does not depends on k_x and the sum over k_x extends over the first Brillouin zone of the effective 1D lattice. The advantage of this formulation is clearly seen from Eq. (11): the surface Green's function is obtained from combinations of full-space Green's functions. For different surface orientations, one simply rotates the full-space Green's function to the appropriate angle. Furthermore, it is also clear that here we have a scheme for studying the effects of interactions and fluctuations in tunneling problems. Essentially one can take these effects into account through the bulk Green's function. Here, however, we shall concentrate on mean-field treatments and defer correlation effects to a separate publication.

It is when dealing with lattices with an anisotropic order parameter that one could most easily appreciate the power of the present formulation. For instance in dealing with *d*-wave superconductors, apart from fitting the boundary conditions (8), α also takes care of the different gap structures for propagation along the reflected path and the fictitious path (such as AO and $A'O$ depicted in Fig. 2). In the presence of reflection symmetry [such as an *s*-wave superconductor, or a *d*-wave superconductor at (100) orientation], since the gap structure as seen by these two paths are identical, the full-space bulk Green's function possesses the symmetry $G(d)=G(-d)$. Therefore α becomes (independent of k_y and ω) universally equal to the identity matrix and Eq. (11) reduces to the familiar form[7,11]

$$g_0=\sum_{-\pi/d\leqslant k_x<\pi/d} G(k_x)\times 2\sin^2(k_xd). \quad (12)$$

For general orientations or when taking into account next nearest neighbor hopping, as noted earlier, there could be more than one hard walls. In these circumstances the surface Green's function must satisfy the boundary condition that it vanishes on all these hard walls simultaneously. For instance, let us consider the (210) case with NN hopping: as depicted in Fig. 1(c) there are two hard walls located at $x=-d$ and $-2d$, where $d=a/\sqrt{5}$. Analogous to the single hard-wall problem, we write the half-space Green's function

$$g(x,x')=G(x,x')-G(x,x_1')\alpha_1(x')-G(x,x_2')\alpha_2(x') \quad (13)$$

with $x_1'=-2d-x'$, $x_2'=-4d-x'$ being the location of the image sources, and α_1, α_2 determined by the boundary conditions

$$g(-d,x')=0=g(-2d,x'). \quad (14)$$

In other words, for the point source at x', each hard wall "generates" an image source on the other side of the surface and introduces an α factor which accounts for the additional boundary conditions. The half-space Green's function is a superposition of contributions from the real and all image sources. To obtain the surface Green's function, one again substitutes $x=x'=0$ into Eq. (13). We note in passing that for arbitrary orientations, the number of hard walls may become too large so that the image method becomes analytically intractable. This is one drawback of current method. We shall further address this issue at the end.

Before proceeding to the applications in the following sections, we comment that the present method is not restricted to square lattices. In Sec. III E we will apply this method to systems involving honeycomb lattices. Indeed our generalized method of image relies only on the possibility of reducing 2D lattices into 1D structures through a Fourier transformation in the transverse direction.

III. TUNNELING SPECTROSCOPY IN HYBRID SYSTEMS

A. Normal metal–*d*-wave superconductors

We first study the *ab*-plane tunneling between a normal metal and a *d*-wave superconductor. The superconductor occupies the half-space $x>0$, modeled by the mean-field Hamiltonian

$$H_R=-\sum_{\langle ij\rangle,\sigma} t_R c_{i\sigma}^\dagger c_{j\sigma}-\sum_{\langle ij\rangle',\sigma} t_R'\, c_{i\sigma}^\dagger c_{j\sigma}$$
$$+\sum_{\langle ij\rangle}\Delta_{ij}(c_{i\uparrow}c_{j\downarrow}-c_{i\downarrow}c_{j\uparrow})+\text{H.c.}, \quad (15)$$

where $\langle ij\rangle$ denotes the nearest neighbors, $\langle ij\rangle'$ the next nearest neighbors (NNN), t_R and t_R' are the corresponding

hopping amplitudes, and Δ_{ij} are the mean-field d-wave pairing amplitude. The normal metal on the left is modeled by the same Hamiltonian but with $\Delta=0$ and with only NN hopping term.

The corresponding 1D structure is easily obtained by Fourier transform the Hamiltonian along the y direction. For example, at (110) orientation if including only NN hopping H_R becomes

$$H_R=\sum_{x_i,k_y,\sigma} -2t_R\cos\left(\frac{k_y a}{\sqrt{2}}\right)c^\dagger_{i\sigma}(k_y)c_{i+1\sigma}(k_y) + \sum_{x_i,k_y} 2i\Delta_0\sin\left(\frac{k_y a}{\sqrt{2}}\right)[c_{i\uparrow}(k_y)c_{i+1\downarrow}(-k_y) + c_{i\downarrow}(-k_y)c_{i+1\uparrow}(k_y)]+\text{H.c.} \quad (16)$$

Here c_i are the electron annihilation operators for the 1D lattice at the ith site [see Fig. 1(b)] and a is the lattice constant of the original 2D lattice. The lattice constant of the 1D lattice is identical to the distance d between two consecutive $(hk0)$ planes. By using the Nambu notation[17]

$$\Psi_i(k_y,t)=\begin{pmatrix} c_{i\uparrow}(k_y,t) \\ c^\dagger_{i\downarrow}(-k_y,t)\end{pmatrix}, \quad (17)$$

H_R can be formally written in the form

$$H_R=\sum_{x_i,k_y}(\Psi^\dagger_i H_{i,i+1}\Psi_{i+1}+\Psi^\dagger_i H_{i,i-1}\Psi_{i-1}) \quad (18)$$

with appropriately defined hopping amplitudes $H_{i,i\pm1}$.

According to the image method as explained in Eq. (9), our task now is to find the full-space Green's function $G(x,x';k_y;\omega)$. If one further performs Fourier transform on x coordinates, one realizes that all we need is to rotate the full-space Green's function to the appropriate angle in accordance to the interface orientations $(hk0)$. In fact, in the momentum space, Eq. (18) has the usual BCS form

$$H_R=\sum_{\mathbf{k}}(c^\dagger_{\mathbf{k}\uparrow}c_{-\mathbf{k}\downarrow})\begin{pmatrix}\epsilon_{\mathbf{k}} & \Delta_{\mathbf{k}} \\ \Delta^*_{\mathbf{k}} & -\epsilon_{\mathbf{k}}\end{pmatrix}\begin{pmatrix} c_{\mathbf{k}\uparrow} \\ c^\dagger_{-\mathbf{k}\downarrow}\end{pmatrix}, \quad (19)$$

except that $\epsilon_{\mathbf{k}}$ and $\Delta_{\mathbf{k}}$ are rotated as

$$\epsilon_{\mathbf{k}}=-2t_R[\cos(\mathbf{k}\cdot\mathbf{a})+\cos(\mathbf{k}\cdot\mathbf{b})]-4t'_R\cos(\mathbf{k}\cdot\mathbf{a})\cos(\mathbf{k}\cdot\mathbf{b}),$$

$$\Delta_{\mathbf{k}}=-2\Delta_0[\cos(\mathbf{k}\cdot\mathbf{a})-\cos(\mathbf{k}\cdot\mathbf{b})], \quad (20)$$

where for $(hk0)$ orientation the lattice vectors $\mathbf{a}=a(\cos\theta, -\sin\theta)$, $\mathbf{b}=a(\sin\theta,\cos\theta)$ with $\theta=\tan^{-1}(k/h)$. The full-space retarded Green's function is then obtained as

$$G(x_i,x_j)=\sum_{-\pi/d\le k_x<\pi/d} G(k_x,k_y,\omega)\times e^{ik_x(x_i-x_j)}, \quad (21)$$

where $G(k_x,k_y,\omega)=[\omega+i\eta-\hat{H}_R(k_x,k_y,\omega)]^{-1}$, with $\hat{H}_R$ the matrix in Eq. (19) and $\eta=0^+$. The half-space bare Green's function g^r_0 is then obtained via Eq. (9).

When the tunneling Hamiltonian is turned on, the half-space Green's functions get renormalized due to tunneling events (see the Appendix). This is expressed as a perturbation series. In the elastic case, it can be re-summed to all orders in t_I.[10] With the assumption that the renormalized advanced and retarded half-space Green's functions satisfy $[g^r_{\alpha\beta}]^\dagger=g^a_{\beta\alpha}$ (where $\alpha,\beta=\{L,R\}$ label the electrodes), we can express the tunneling current as

$$I=I_1+I_2+I_3+I_A, \quad (22)$$

where

$$I_1=\sum_{k_y} 4\pi e\int_{-\infty}^{\infty}d\omega\ \ t_I^2[f(\omega-eV)-f(\omega)] \times A_{L,11}(\omega-eV)A_{R,11}(\omega)|1+t_I g^r_{RL,11}(\omega)|^2, \quad (23)$$

$$I_2=\sum_{k_y} -8\pi e\int_{-\infty}^{\infty}d\omega\ \ t_I^2[f(\omega-eV)-f(\omega)]A_{L,11}(\omega-eV) \times\text{Re}\{A_{R,12}(\omega)(t_I g^a_{LR,21}(\omega)[1+t_I g^r_{RL,11}(\omega)])\}, \quad (24)$$

$$I_3=\sum_{k_y} 4\pi e\int_{-\infty}^{\infty}d\omega\ \ t_I^4[f(\omega-eV)-f(\omega)]A_{L,11}(\omega-eV) \times A_{R,22}(\omega)|g^r_{RL,12}(\omega)|^2, \quad (25)$$

$$I_A=\sum_{k_y} 4\pi e\int_{-\infty}^{\infty}d\omega\ \ t_I^4[f(\omega-eV)-f(\omega+eV)]A_{L,11} \times(\omega-eV)A_{L,22}(\omega+eV)|g^r_{RR,12}(\omega)|^2. \quad (26)$$

Here $f(\omega)$ is the Fermi function and

$$A_\alpha=i/(2\pi)(g^r_{0,\alpha\alpha}-g^{r\,\dagger}_{0,\alpha\alpha}) \quad (27)$$

are the spectral weight matrices for $\alpha=\{L,R\}$. The indices 1, 2 in the Green's functions and the spectral weight matrices refer to the particle and the hole components, respectively. $t_I=t_I(\omega,k_y)$ is the tunneling amplitude between the two electrodes. It is remarkable that the expression for I_2 here generalizes that found in Ref. 7 and is applicable to any interface orientation. For the special cases considered in Ref. 7, where the surface Green's functions are symmetric [for (100) orientation] or antisymmetric [for (110) orientation], Eq. (24) reproduces previous results. From these formulas one can clearly identify the contributions from each channel in the tunneling process. In particular, I_1 is the contribution from single particle tunneling and I_A the Andreev reflection (thus I_A depends on the particle and hole components of the spectral weight matrix A_L).

We now present some of our results. Figure 3 shows the tunneling spectra for (110) and (210) orientations at the doping levels $\delta=0.08$, 0.14, and 0.20. Here we study the doping dependence by resorting to the mean-field slave boson theory for the t-t'-J model.[7] The electron operators c and $c^\dagger$ are then essentially the spinon operators and the Green's function for spinons as well. The holons condense so that $\langle b\rangle=\sqrt{\delta}$. The mean-field parameters t_R, t'_R, Δ_0, and the chemi-

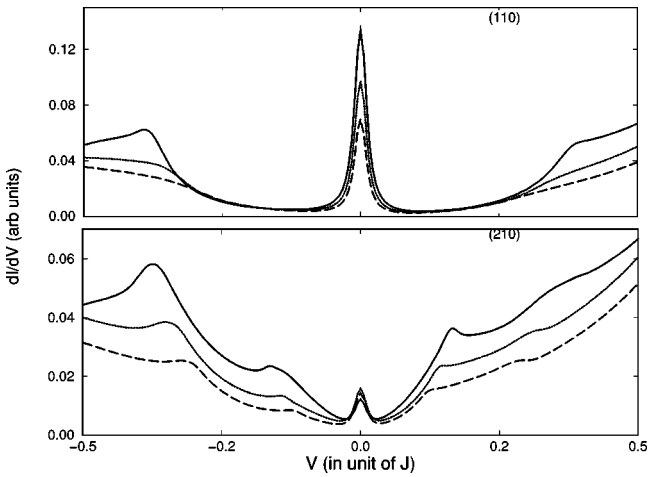

FIG. 3. The total differential conductance for (110) and (210) interfaces at dopings $\delta=0.08$ (solid lines), 0.14 (dotted lines), and 0.20 (dash lines). The weak link is modeled by the interface hopping $t_I(\omega)=\exp[-\sqrt{(\omega_0-|\omega|)/\Gamma}]$. Here we use $\omega_0=11\Delta_0$ and $\Gamma=\Delta_0$.

cal potential μ_R for each doping are calculated self-consistently.[7] It is obvious from Fig. 3 that the ZBCP is significantly reduced in the (210) orientation. Interestingly, for (110) orientation the ZBCP decreases upon increasing doping while for (210) case it grows and then falls with doping. Another interesting feature in the tunneling spectra is the subgap structures near $\pm 2\Delta_0$ in the (210) case. These may have originated from resonances due to broken surface pairs, resulting from the dangling bonds in (210) orientations.[18]

The ZBCP originates from zero-energy surface states (or the midgap states) due to Andreev reflections. In our formulation these states arise from singularities in the image contributions which manifest as poles in the α factors. In the presence of a single hard wall, the poles are determined by the zeros of the following factor when $\eta=0$:

$$\beta(k_y)=\det[G(d;k_y,\omega=0)]. \tag{28}$$

This produces singular behavior in the Green's functions and results in the ZBCP. In the (100) case, since α_0 is simply the identity matrix the surface Green's function (12) is regular at $\omega=0$ thus there is no ZBCP.

B. Tunneling into current-carrying superconductors

We now extend previous results by considering tunneling into current-carrying superconductors. In experiments one applies magnetic field along the *c*-axis of the superconductor, so that a screening current is generated over the *ab* plane. When a quasiparticle tunnels across the surface layer, it acquires additional energy from the supercurrent. Thus the zero-energy surface state evolves in this case into two surface states with non-zero energy. In the tunneling spectra this appears as ''splitting'' of the ZBCP (Fig. 4). Fogelström *et al.* have analyzed the splittings in the continuum limit.[19] Here we examine the tunneling spectra base on our discrete model.

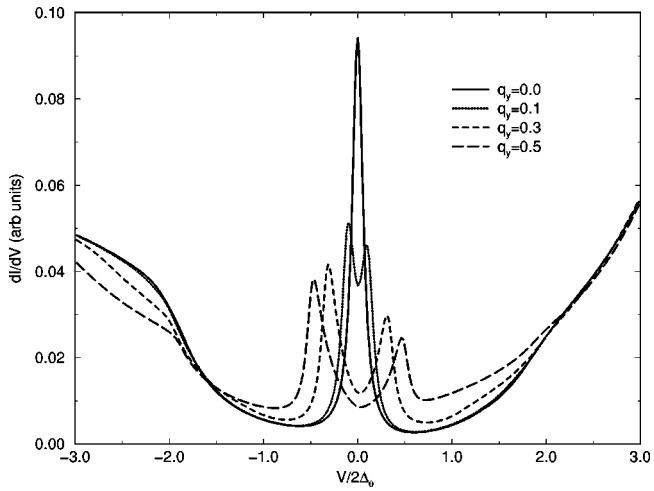

FIG. 4. Splitting of the ZBCP for various values of q_y (for $\delta=0.16$).

To marry with formulations in the previous section, we note that in the presence of supercurrent the gap function is modified as[20] $\Delta_{ij}\rightarrow\Delta_{ij}\exp[i\mathbf{q}\cdot(\mathbf{r}_i+\mathbf{r}_j)]$, where $\mathbf{q}=(0,q_y)$ is the superfluid momentum and is proportional to the magnetic field. We shall assume that tunneling events take place only within a shallow layer of order about the penetration depth from the surface, so that q_y is approximately uniform in the region of our concern. This additional phase can be absorbed into the electron operator by the transformation $c_{i\sigma}\rightarrow c_{i\sigma}\exp(i\mathbf{q}\cdot\mathbf{r}_i)$. In Fourier space the Hamiltonian becomes

$$H_R=\sum_{\mathbf{k}}\begin{pmatrix} c^{\dagger}_{\mathbf{k}\uparrow} & c_{-\mathbf{k}\downarrow}\end{pmatrix}\begin{pmatrix}\epsilon_{\mathbf{k}+\mathbf{q}} & \Delta_{\mathbf{k}}\\ \Delta^{*}_{\mathbf{k}} & -\epsilon_{\mathbf{k}-\mathbf{q}}\end{pmatrix}\begin{pmatrix} c_{\mathbf{k}\uparrow}\\ c^{\dagger}_{-\mathbf{k}\downarrow}\end{pmatrix}, \tag{29}$$

where $\epsilon_{\mathbf{k}}$ and $\Delta_{\mathbf{k}}$ are given by Eq. (20). The momentum space Green's function that is fed into Eq. (11) is obtained in the same way: $G(k_x,k_y,\omega)=[\omega+i\eta-\hat{H}_R(k_x,k_y,\omega)]^{-1}$, with $\hat{H}_R$ the matrix in Eq. (29).

Figure 4 shows typical tunneling spectra for the splitting of the ZBCP when increasing q_y. Note that the slightly asymmetric splitting originates from the particle-hole asymmetry in $\epsilon_{\mathbf{k}}$. Figure 5 plots the magnitude of the splitting versus the applied magnetic field for underdoped case. For small $\mathbf{q}$, the quasiparticle energy $E^{(\pm)}_{\mathbf{k}}=\pm E_{\mathbf{k}}+\mathbf{q}\cdot\partial\epsilon_{\mathbf{k}}/\partial\mathbf{k}$ to the leading order, where $E_{\mathbf{k}}=\sqrt{\epsilon^2_{\mathbf{k}}+\Delta^2_{\mathbf{k}}}$. This leads to linear splitting of the ZBCP, as observed in small applied fields. For higher fields, one has to retain the full $\mathbf{q}$ dependence, resulting in the bending of the splitting. This is purely due to the lattice effect. Also shown in Fig. 5 are the results taking into account suppression of the superconducting gap under magnetic fields self-consistently. The curve is seen to be ''pushed'' inwards while maintaining similar features. Note that quantitative agreement with experimental observations[21,22] can be obtained by fitting scales of our results to the experimental data.[16] Nevertheless, we did not observe any zero-field splitting at overdoping. This is in contrast with the experiment of Ref. 22, where it is attributed to the change of the pairing symmetry.

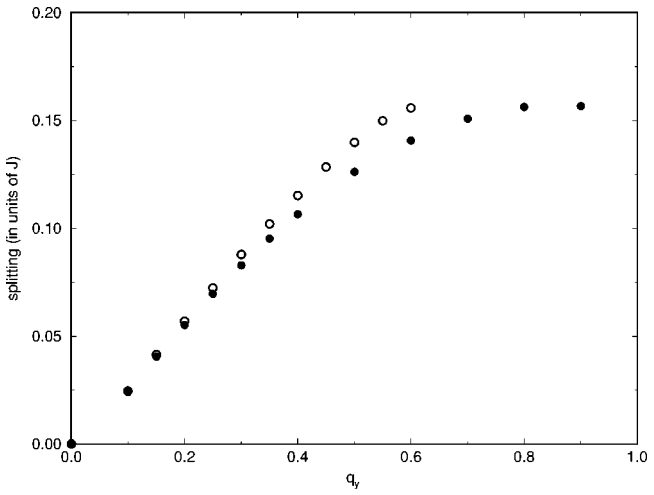

FIG. 5. The dependence of splitting on magnetic field for doping $\delta=0.12$. The empty and full symbols represent data calculated, respectively, with and without self-consistently taking into account the magnetic fields in solving the t-t'-J slave boson mean-field equations. In the former case, the superconducting gap is strongly suppressed when $q_y \geqslant 0.65$, where difficulty in convergence of the mean-field solution arises.

The doping dependence of splitting is also shown in Fig. 6 for $q_y=0.15$ and 0.80, which are respectively in the linear and the saturated regimes in Fig. 5. Note that the splitting increases with doping, in agreement with Ref. 22.

In passing we point out that the splitting depends sensitively on the Fermi surface topology. Indeed for $\mu_R=0$ we find no splitting of the ZBCP whatever the value of q_y is. One can confirm this analytically by making an asymptotic expansion of the Green's function around $\omega=0$. At $\mu_R=0$ one finds the conductance peak invariantly stays at the zero bias.

C. Polyacetylene

Up to this point, we have considered tunnel junctions with superconducting test electrodes, where particles of opposite

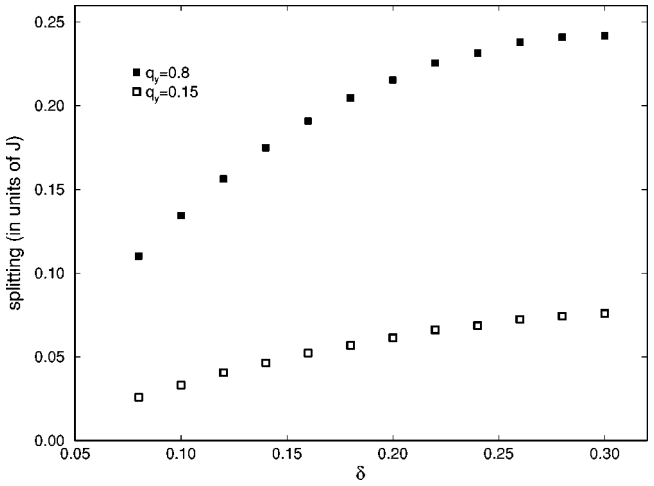

FIG. 6. Splitting versus dopings for $q_y=0.15$ (open squares) and 0.8 (solid squares).

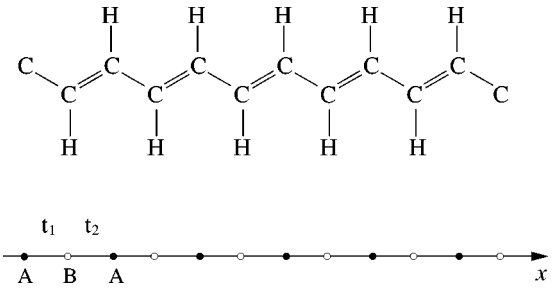

FIG. 7. The structure of polyacetylene and the 1D t_1-t_2 model. Filled and empty circles are lattice points over the A and B sublattices.

spins form pairs. In this and the following sections we will consider systems which exhibits particle-hole pairing over bipartite lattices. We shall start by first considering a simple 1D model based on the structure of polyacetylene.[23] This will turn out to be very helpful for understanding results in the following sections. Most importantly, it provides the criteria for the formation of midgap states in semi-infinite bipartite systems.

The model we shall examine here is a 1D chain with alternating hopping amplitudes t_1, t_2 as shown in Fig. 7. The separation between the lattice points is taken to be a constant a.[24] It is convenient to categorize the lattice points into A and B sublattices and express the Hamiltonian for this t_1-t_2 model as

$$H_R=\sum_{i_B,\sigma} -t_1 c_{i-1}^{A\dagger} c_i^B - t_2 c_i^{B\dagger} c_{i+1}^A + \text{H.c.} \tag{30}$$

Here c_i^α annihilates electrons over site i on the $\alpha=\{A,B\}$ sublattice (spin indices σ will be omitted throughout), and the sum run over sites i in the B sublattice only. In the momentum space, one finds

$$H_R=\sum_{k,\sigma} (c_k^{A\dagger} \quad c_k^{B\dagger}) \begin{pmatrix} 0 & \Lambda_k \\ \Lambda_k^* & 0 \end{pmatrix} \begin{pmatrix} c_k^A \\ c_k^B \end{pmatrix}, \tag{31}$$

where $\Lambda_k=-(t_1+t_2)\cos(ka)-i(t_1-t_2)\sin(ka)$. It is easily seen that the quasiparticle energy are given by $\pm|\Lambda_k|$. Note that $\mathrm{Re}\{\Lambda_k\}$ plays the role of the hopping energy, while $\mathrm{Im}\{\Lambda_k\}$ is the pairing between particles and holes. Since $\mathrm{Im}\{\Lambda_k\} \propto t_1-t_2$, a gap opens at the chemical potential when $t_1 \neq t_2$.

For semi-infinite chains, there are two possible configurations with the terminating site being an A or a B sublattice point. In either case we choose the boundary point the origin $x=0$ and construct the surface Green's function as follows:

$$g_0=G(0,0)-G(0,-2a)G^{-1}(-a,-2a)G(-a,0). \tag{32}$$

Here the appropriate component of the Green's functions should be used in accordance with the coordinates. This depends the type of the end point. For instance, for an A-type boundary, even/odd sites are attributed to the A/B sublattices. Therefore, terms such as $G(-a,-2a)$ in Eq. (32)

should be expressed as $G_{BA}(-a,-2a)$. One can formally keep track of the A/B sublattice nature by defining the retarded Green's function as

$$G(x_i^\alpha,t;x_j^\beta,0)=-i\Theta(t)\langle\{c_i^\alpha(t),c_j^{\beta\dagger}(0)\},\rangle, \tag{33}$$

where α is the index for the sublattice. In the Fourier space, one has

$$G(x_i^\alpha,x_j^\beta;\omega)=\sum_{-\pi/2a\leqslant k_x<\pi/2a} G_{\alpha\beta}(k,\omega)\times e^{ik(x_i^\alpha-x_j^\beta)}. \tag{34}$$

Here by inverting the matrix $\omega+i\eta-\hat{H}_R(k,\omega)$, we obtain

$$G_{\alpha\beta}(k,\omega)=\frac{1}{(\omega+i\eta)^2-E_k^2}\begin{pmatrix}\omega+i\eta & \Lambda_k\\ \Lambda_k^* & \omega+i\eta\end{pmatrix}_{\alpha\beta}, \tag{35}$$

where the matrix indices are assigned according to the convention used in Eq. (31).

From Eq. (32), one sees that the only possible source of singular behavior in g_0 resides in the inverse part $G^{-1}(-a,-2a)$. The existence of the zero-energy mode thus depends on the behavior of $G(-a,-2a)$ at $\omega=0$. This is analogous to the ND junctions where the ZBCP results from the zeros of the determinant $\beta(k_y)$, Eq. (28). For example, in the case of *A*-type boundaries, by setting $\eta=\omega=0$ and $\alpha=2,\beta=1$ in Eq. (35), we find that $G(-a,-2a)$ can be expressed as a simple contour integral and has the following behavior:

$$G_{BA}(-a,-2a;\omega=0)=\begin{cases}0 & \text{if } t_1<t_2,\\ 1/2t_1 & \text{if } t_2<t_1.\end{cases} \tag{36}$$

Thus the condition for the existence of ZBCP is $t_1<t_2$ as in this case, G_{BA}^{-1} diverges. In the following sections we shall see that this provides for 2D bipartite systems a general criterion for the range of transverse momenta k_y where zero-energy states exist. For *B*-type boundary the analysis is identical, except an exchange in the roles of t_1 and t_2. Therefore when the ZBCP shows up in an *A*-type chain, it must be absent in a *B*-type chain, and vice versa. This is shown in Fig. 8 for the case of polyacetylene. The current expression here is identical to Eq. (39) given in the following section, except the extra sum over k_y there.

D. Normal metal–*d*-density wave states

In underdoped cuprate superconductors, it is observed in experiments that there are signatures of a ''partial'' gap well above the superconducting temperature T_c. This anomalous regime is termed the pseudogap phase.[25] Experiments also find that the pseudogap is consistent with a *d*-wave structure. Recently Chakravarty *et al.* proposed that the pseudogap phase is possibly the *d*-density-wave (DDW) state.[26] It is therefore of interest to examine the tunneling spectra of normal-metal–*d*-density-wave (N-DDW) junctions.

The DDW state is characterized by the staggered flux in the elementary plaquettes of the lattice. The bond currents

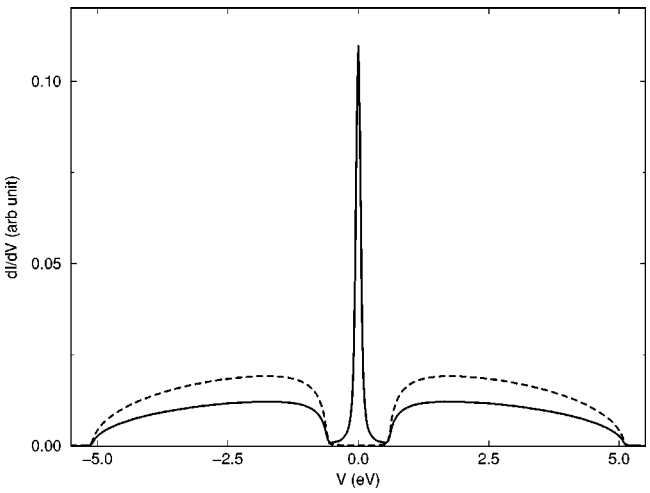

FIG. 8. Typical tunneling conductance curves for polyacetylene with *A* type (solid line) and *B* type (dashed line) end points. Here $t_1=2.25$ eV and $t_2=2.85$ eV; thus the bandwidth is $t_1+t_2=5.1$ eV and the gap width $|t_1-t_2|=0.6$ eV. The linear chain on the left side is a wideband material and the tunneling amplitude H_T is $t_I=0.3$.

circulating the unit cell of the underlying square lattice break, among other symmetries, the invariance of translation by one lattice spacing and lead to a bipartite structure (Fig. 9). Obviously, if the interface cuts at (110) direction, the reflection symmetry is broken—in contrast to the (100) case. Therefore, we shall examine the (110) direction with the following mean-field Hamiltonian:

$$H_R=\sum_{i_B,\sigma}\{\chi(c_{i+\mathbf{a}}^{A\dagger}c_i^B+c_{i-\mathbf{a}}^{A\dagger}c_i^B)+\chi^*(c_{i+\mathbf{b}}^{A^\dagger}c_i^B+c_{i-\mathbf{b}}^{A\dagger}c_i^B) +\text{H.c.}\}, \tag{37}$$

where c_i^α annihilates an electron at site i over the α sublattice, and χ is the hopping amplitude on the bond [Fig. 9(b)]. Making the Fourier transformation along the y direction in H_R, one finds

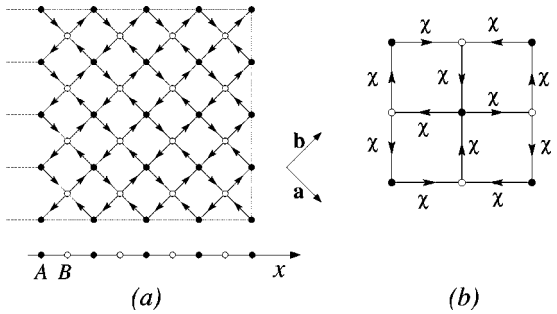

FIG. 9. (a) The *d*-density-wave state in (110) orientation and its corresponding 1D model. Filled and empty circles label the *A* and *B* sublattices; the arrows indicate the directions of bond currents. Dashed lines extended from the boundary sites indicate the coupling of the tunneling Hamiltonian. (b) shows explicitly the bond variables in a doubled unit cell.

$$H_R = \sum_{x_i^B, k_y, \sigma} \{\Lambda_{i,i-1} c_{i-1}^{A\dagger}(k_y) c_i^B(k_y) + \Lambda_{i,i+1} c_i^{B\dagger}(k_y) c_{i+1}^A(k_y) + \text{H.c.}\}, \quad (38)$$

where $\Lambda_{i,i\pm1} = 2\,\text{Re}\{\chi e^{\pm i k_y a/\sqrt{2}}\}$ with a being the lattice constant of the square lattice. One sees that this belongs to the class of the t_1-t_2 model defined in Eq. (31) except that now $\Lambda_{\mathbf{k}} = \epsilon_{\mathbf{k}} + i\Delta_{\mathbf{k}}$ with $\epsilon_{\mathbf{k}}$ and $\Delta_{\mathbf{k}}$ being given by Eq. (20) where one sets $t_R = -\text{Re}\{\chi\}$, $\Delta_0 = -\text{Im}\{\chi\}$, and $t_R' = 0$.

To find the tunneling current we apply again the Keldysh formulation outlined in the Appendix. For fixed k_y the full-space retarded Green's function $G(x_i^\alpha, t; x_j^\beta, 0; k_y)$ is obtained similar to its 1D counterpart. The momentum space Green's function has the same form as given in Eq. (35) (with k replaced by $\mathbf{k}$) and the inverse Fourier transformation is carried out as in Eq. (34) with here $-\pi/2d \leqslant k_x < \pi/2d$, where $d = a/\sqrt{2}$ is the lattice spacing of the effective 1D structure.

From the bulk Green's function, one can again construct the half-space surface Green's function using the method of image. The current expressions here, however, are distinct from those of Eqs. (23)–(26). Indeed since we are dealing with a single component Green's function the calculation is much simpler than previously. As shown in the Appendix, the current expression is here

$$I = \sum_{k_y, \sigma} 2\pi e \int_{-\infty}^{\infty} d\omega t_I^2 [f(\omega - eV) - f(\omega)] \times A_L(\omega - eV) A_R(\omega) |1 + t_I g_{RL}^r(\omega)|^2. \quad (39)$$

This is exactly the single-particle current I_1 of Eq. (23) for ND tunneling. There is no contribution from ''Andreev reflections'' in N-DDW tunneling. This is due to the fact that in the DDW state the pairing takes place between particles and holes of momenta $\mathbf{k}$ and $\mathbf{k}+\mathbf{Q}$, with $\mathbf{Q}$ the nesting vector of 2D square lattices. Thus the Andreev reflected particles are still electrons whose response to the bias voltage are the same as the incident particles; as a result their contributions to the tunneling current cancel exactly. In the ND junction, however, a particle is Andreev reflected as a hole, which behaves *oppositely* under applied bias. Figure 10(a) shows a typical plot for differential conductance versus voltage for N-DDW junctions. The conspicuous ZBCP agrees with recent calculations done by Honerkamp and Sigrist.[27]

The reason for the ZBCP here can be understood on the basis of the results in the previous section. Just like polyacetylene, the midgap states arises when g_0 is singular due to the zeros in the Green's function such as in Eq. (36). For each k_y Eq. (38) resembles the t_1-t_2 model with $t_1 = -\Lambda_{i,i-1}$ and $t_2 = -\Lambda_{i,i+1}$. Therefore, for example, for A-type boundary one expects midgap states for the range of k_y where $\Lambda_{i,i-1} > \Lambda_{i,i+1}$, or $\text{Im}\{\chi\}\sin(k_y a/\sqrt{2}) > 0$. Since here $\text{Im}\{\chi\} = -\Delta_0 < 0$, this leads to $-\sqrt{2}\pi/a < k_y < 0$.

We have so far considered only the case of vanishing chemical potential μ_R in the DDW state. At finite chemical potential the grand Hamiltonian for the DDW is $K_R = H_R - \mu_R N_R$. Hence $-\mu_R N_R$ is diagonal and simply shifts the excitation energy by $-\mu_R$. As a result, a shift $\omega \to \omega + \mu_R$ is induced in the Green's function. This is in sharp contrast with the ND case; there the chemical potential shifts the quasiparticle energy $\epsilon_{\mathbf{k}} \to \epsilon_{\mathbf{k}} - \mu_R$ in the Green's function but not the frequency. This results in the distinct behavior of the ZBCP for ND and N-DDW junctions at finite μ_R. For N-DDW junctions since $\omega \to \omega + \mu_R$ at finite chemical potential, the conductance peak is shifted from zero bias to the opposite value of the chemical potential $-\mu_R$. For ND junctions, however, the midgap state stays at $\omega = 0$ even at finite chemical potential, thus the conductance peak always position at zero bias (see Fig. 3). This shift has an obvious implication: the peak will split due to the Zeeman splitting (see Fig. 10). The orbital effects of magnetic fields can be included by changing χ into $\chi e^{i\mathbf{q}\cdot(\mathbf{r}_i - \mathbf{r}_j)}$ for any nearest neighbor sites i, j. This takes into account the current induced near the interface. Since under this change both $\epsilon_{\mathbf{k}}$ and $\Delta_{\mathbf{k}}$ undergo shifting of $\mathbf{k}$ by $\mathbf{q}$ which can be absorbed into the summation of $\mathbf{k}$, the peak does not split. Therefore, the splitting of ZBCP turns out the same for both in-plane and perpendicular magnetic fields. This is in contrast to the ND junction where orbital effects dominate for perpendicular fields.

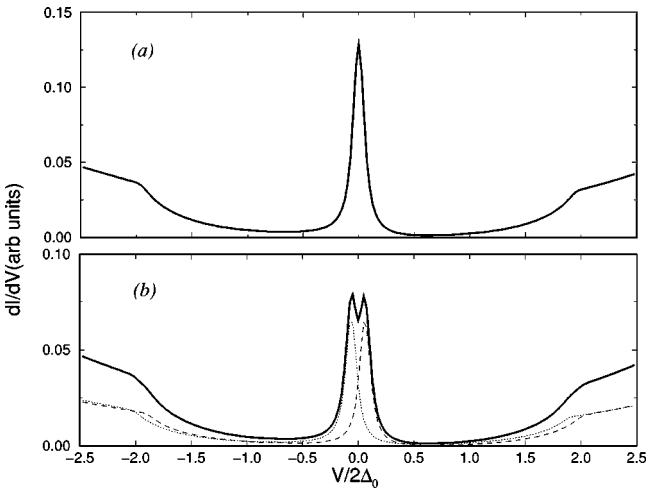

FIG. 10. Typical conductance (dI/dV) curves for N-DDW junctions at (110) orientation in the (a) absence and (b) presence of *in-plane* magnetic field. Here the boundary surface consists of A sublattice sites and $\chi = (-t_R - i\Delta_0) = (-0.447 - 0.1i)$, $\eta = 0.01$. Also shown in (b) are contributions from the spin-up (dashed line) and spin-down (dotted line) components. The Zeeman splitting is here $0.24\ \Delta_0$. The weak link is modeled by the same expression as in Fig. 3.

In closing this section we note that since the next n.n. term t_R' couples only lattice sites within each sublattice, its effect is similar to that of the chemical potential. Therefore, t_R' cause the ZBCP and the spectrum to migrate when $t_R' \neq 0$. This is displayed in Fig. 11.

E. Graphite sheets

So far we have considered systems involving only square lattices. As commented in the end of Sec. II, our formulation is general and can be applied to any systems which can be projected into 1D structures. As an example, we study in this

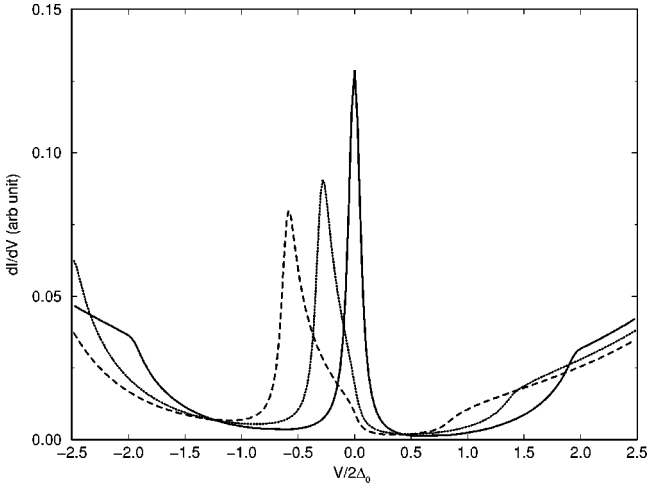

FIG. 11. Same as Fig. 10(a) but with next n.n. hopping amplitudes $t_R'=0.0$ (solid line), -0.03 (dotted line), and -0.06 (dashed line).

section the in-plane tunneling from a normal metal into semi-infinite graphite sheets (NG junctions).

In the tight-binding limit the Hamiltonian for the bulk graphite sheet is

$$H_R=\sum_{i_B,\sigma}-\gamma_0 c_{i+\mathbf{a}}^{A\dagger}c_i^B-\gamma_1 c_{i+\mathbf{b}}^{A\dagger}c_i^B-\gamma_2 c_{i-\mathbf{a}-\mathbf{b}}^{A\dagger}c_i^B+\text{H.c.} \tag{40}$$

Here the lattice is divided into A and B sublattices, **a**, **b** are the lattice vectors illustrated in Fig. 12, and γ_i are the hopping integrals for π bands. For simplicity we shall take $\gamma_0=\gamma_1=\gamma_2$ in the following. We will be interested in two orientations of the lattice: one with zigzag and the other with armchair boundaries.

We first consider the zigzag case and choose the frame of coordinates as shown in Fig. 12(a). Fourier transformation in the transverse direction leads to 1D Hamiltonian which resembles Eq. (30)

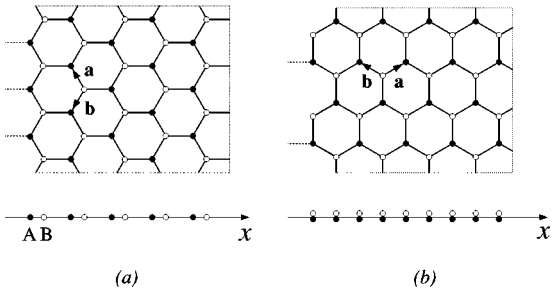

FIG. 12. Graphite sheets with (a) zigzag and (b) armchair boundaries and the corresponding 1D models after k_y transformation. Filled and empty circles represent respectively the A and B sublattices; **a**, **b** are lattice vectors. The dashed lines draw from the boundary sites indicate connections to the left electrode through the tunneling Hamiltonian similar to Fig. 1(a).

$$H_R=\sum_{x_i^B,k_y,\sigma}-t_1 c_{i-1}^{A\dagger}(k_y)c_i^B(k_y)-t_2 c_i^{B\dagger}(k_y)c_{i+1}^A(k_y)+\text{H.c.} \tag{41}$$

with

$$t_1=2\gamma_0\cos\left(\frac{\sqrt{3}}{2}k_y a\right)\quad\text{and}\quad t_2=\gamma_0, \tag{42}$$

a being the lattice constant. Further k_x transformation brings H_R into the same form as Eq. (31) with $\Lambda_{\mathbf{k}}=-\gamma_0\{e^{-ik_x a}+2\cos[(\sqrt{3}/2)k_y a]e^{ik_x a/2}\}$.

In applying the method of image, we note that the projected 1D lattice for the zigzag case has alternating bond length, which breaks the reflection symmetry and hence implies the possible existence of the ZBCP. The alternating bond length, however, seems to cause difficulty in locating the image point of an arbitrary source site. For instance, the usual choice—the mirror image—does not always put the image point right on the lattice. Nevertheless, since in 1D the hard wall becomes a point, as long as the Green's function propagating from the real source to the hard wall can be canceled by that from a fictitious source, so that the boundary condition is satisfied, uniqueness of the half-space Green's function implies that the location of the fictitious source can be chosen at will. Indeed, this can be explicitly checked numerically. To be definite, we shall place the fictitious source at $x=-(3/2)a$ and apply the method of image. The boundary condition $g(-a,x')=0$ for all x' immediately leads to

$$g_0=G_{AA}(0,0)-G_{AA}(0,-3/2a)\times G_{BA}^{-1}(-a,-3/2a)G_{BA}(-a,0). \tag{43}$$

Here we have labeled the attributes of the lattice points explicitly in the subscripts of the Green's functions. Just like polyacetylene, the midgap states arise when g_0 is singular, namely at the zeros of $G_{BA}(-a,-3/2a)$ when $\eta=0$. From Eq. (42) the correspondence to the t_1-t_2 model indicates that midgap states exist for k_y which satisfy $\cos(k_y\sqrt{3}a/2)<1/2$. When setting $\sqrt{3}a=1$ we find $-\pi\leqslant k_y<-2\pi/3$ or $2\pi/3<k_y\leqslant\pi$, exactly what is found in band structure calculations.[28]

For the zigzag orientation, apart from the zigzag boundary, there could also be the "bearded" boundary where the surface layer consists of B sites. This is reminiscent of the case of B-type end point of the t_1-t_2 model. A similar analysis as above can also be used here. We find in this case the zero-energy state arises when $(\sqrt{3}a=1)$ $-2\pi/3<k_y<2\pi/3$. The current expression are the same as Eq. (39) for N-DDW junctions. The corresponding tunneling spectra are shown in Fig. 13.

Let us now consider the armchair case [Fig. 12(b)]. After the Fourier transformation along the interface, one finds

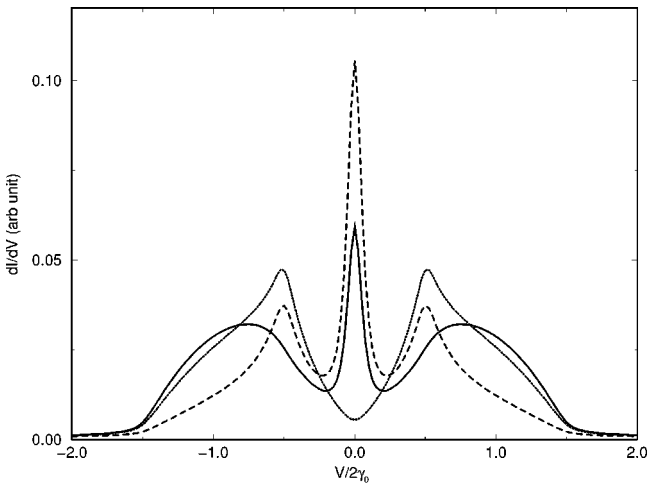

FIG. 13. Typical tunneling conductance curves for NG junctions with zigzag (solid line), bearded (dashed line), and armchair (dotted line) boundaries. Here $\gamma_0=0.1$ and the left electrode is a wideband metal. The weak link is modeled by the same expression as in Fig. 3 with here $\omega_0=11\gamma_0$ and $\Gamma=\gamma_0$.

$$H_R=\sum_{x_i^B,k_y,\sigma}-\gamma_0[c_i^{B\dagger}(k_y)c_i^A(k_y)e^{-ik_ya}+c_i^{B\dagger}(k_y)c_{i+1}^A(k_y)e^{ik_ya/2}+c_i^{B\dagger}(k_y)c_{i-1}^A(k_y)e^{ik_ya/2}+\text{H.c.}]. \tag{44}$$

Note that both A and B components exist for each site x_i as shown in Fig. 12(b). The propagation between x_i and x_j thus compose of four components and the full-space Green's function form a 2×2 matrix

$$G(x_i,x_j)=\begin{pmatrix} G(x_i^A,x_j^A) & G(x_i^A,x_j^B) \\ G(x_i^B,x_j^A) & G(x_i^B,x_j^B)\end{pmatrix}. \tag{45}$$

Further k_x transformation yields the Hamiltonian (31) with here

$$\Lambda_{\mathbf{k}}=-\gamma_0\left[e^{ik_ya}+2\cos\left(\frac{\sqrt{3}}{2}k_xa\right)e^{-ik_y(a/2)}\right]. \tag{46}$$

Note that $\Lambda(-k_x,k_y)=\Lambda(k_x,k_y)$ implies that reflection symmetry is preserved here. Similar to the case of polyacetylene, in momentum space, $G(\mathbf{k},\omega)$ has exactly the same form as Eq. (35). However, now the hard-wall boundary condition becomes a matrix equation

$$g(x_i^\alpha,x_j^\beta)|_{x_i=-d}=0 \quad \text{for all } \alpha,\beta=\{A,B\}, \tag{47}$$

where $d=(\sqrt{3}/2)a$ is the lattice constant of the projected 1D lattice. The surface Green's function then takes the form

$$g_0=G(0,0)-G(0,-2d)G^{-1}(-d,-2d)G(-d,0). \tag{48}$$

Since translational symmetry is preserved in this 1D lattice, we have $G(-d,-2d)=G(d)$ and $G(-d,0)=G(-d)$. Reflection symmetry implies $G(d)=G(-d)$ and consequently

$$g_0=G(0)-G(2d). \tag{49}$$

In this case, one thus expects no midgap states.

Without loss of generality, we connect the A sublattice to the left side [Fig. 12(b)]. The current expression is then the same as Eq. (39), where g_0 is replaced by the 11 (or AA) component of Eq. (49). The conductance curve for this case is also shown in Fig. 13.

IV. DISCUSSIONS AND CONCLUSIONS

In conclusion, the generalized method of image that we developed allows us to deal with various tunneling problems in a unified manner, with full tight-binding nature being taken into account. In particular, applying our method to investigate the splitting of ZBCP in normal metal–d-wave superconductor junction under magnetic fields yields results in agreement with recent experiments. Furthermore, we predict that a sharp conductance peak at the chemical potential in the tunneling spectra should exist for tunneling into the d-density-wave state at (110) orientation. This peak will shift away from the chemical potential if the next nearest neighbor hopping t_R' exists, which also offers a way to measure t_R'. Under in-plane magnetic fields, it also splits due to Zeeman splitting. These provide signatures to be looked for in experiments, especially in normal-metal–pseudogap-cuprate junctions for testing the proposal of Ref. 26.

The general applicability of our formulation is further demonstrated by considering tunneling into graphite sheets at the zigzag and armchair orientations, and it shows complete agreement with findings in the study of graphite ribbons by direct computation of energy spectrum.[28]

The merit of our formulation lies in two aspects. First, it offers a unified method for theoretical study of the tunneling spectroscopy of various junction systems. Secondly, as already pointed out at the beginning of the paper our method allows us to express what is being measured in tunneling experiments in terms of bulk Green's function. For instance, in a single hard-wall configuration, if a wideband metal is used for the left part, in the tunneling limit ($t_I\ll1$), tunneling experiments essentially measure the *surface* density of state given by Eq. (3), which as we have seen, can be expressed in terms of two contributions from the bulk [see Eq. (1)]. The role of reflection is further manifested. Only when the reflection symmetry is broken with respect to the interface, singular behavior may arise from the image part, resulting the ZBCP.

Finally, we discuss a potential drawback of our formulation. This regards dealing with the high-index interfaces: $(hk0)$, where h or k is large. As mentioned at the end of Sec. II B, the number of hard walls required then becomes very large so that the image method is impractical. For instance, the high-index interface, $h=12$ and $k=13$, seems to be a good approximation to the low-index interface (110), and yet the former requires 13 hard walls. From a mathematical point of view, this indeed poses a limitation of our formulation. Nevertheless, since in reality high-index interfaces tend to form small low-index terraces separated by steps, one can apply the image method to each terrace but now using k_y's

that are consistent with the width of the terrace and sum currents from each terrace to obtain the total current. This would be an approximated way to deal with high-index interfaces.

ACKNOWLEDGMENTS

The authors would like to thank Professors Sungkit Yip, Hsiu-Hau Lin, T. K. Lee, Hu Xiao, and C. C. Chi for useful discussions. This research was supported by NSC of Taiwan.

APPENDIX: CURRENT EXPRESSIONS

In this appendix we outline techniques for calculating the tunneling currents for the ND and the N-DDW junctions. We shall start from the expression (7) for the tunneling current.

1. ND junctions

Let us start with the Nambu representation used for the ND junction

$$\Psi_\alpha(x_i,k_y,t)=\begin{pmatrix}\Psi_{\alpha,1}\\ \Psi_{\alpha,2}\end{pmatrix}=\begin{pmatrix}c_{\alpha\uparrow}(x_i,k_y,t)\\ c^\dagger_{\alpha\downarrow}(x_i,-k_y,t)\end{pmatrix}, \tag{A1}$$

where $\alpha=\{L,R\}$ labels the electrodes and the upper and lower elements are associated with, respectively, electrons and holes. The Keldysh non-equilibrium Green's functions are then defined as[29,8]

$$g^{-+}_{\alpha\beta,\mu\nu}(x_i,t;x_j,t')=+i\langle\Psi^\dagger_{\beta,\nu}(x_j,t')\Psi_{\alpha,\mu}(x_i,t)\rangle, \tag{A2}$$

$$g^{+-}_{\alpha\beta,\mu\nu}(x_i,t;x_j,t')=-i\langle\Psi_{\alpha,\mu}(x_i,t)\Psi^\dagger_{\beta,\nu}(x_j,t')\rangle. \tag{A3}$$

For brevity we have suppressed the k_y dependence. The Green's functions here carry the left right indices $\alpha,\beta=\{L,R\}$, the Nambu (spinor) indices $\mu,\nu=\{1,2\}$, and the Keldysh indices $\{-,+\}$. For notational clarity we shall in the following frequently omit irrelevant indices and keep track of only those related to our discussion.

In this representation we define the tunneling matrix $\hat{t}_I\equiv t_I\tau_3\sigma_3$, where τ_3 and σ_3 are the third Pauli matrices pertaining to the Nambu space and the Keldysh space, respectively. In particular, σ_3 is chosen so that in the Keldysh space $\sigma_3^{--}=1=-\sigma_3^{++}$, and $\sigma_3^{-+}=0=\sigma_3^{+-}$, since we have assigned the forward time path the "$-$" time axis, and the return time-path the "$+$" time axis. In the following we will consider only real valued t_I and hence $t_I^*=t_I$.

The current expression (7) can now be written as

$$I(t)=+e\sum_{k_y}\int_{-\infty}^{\infty}\frac{d\omega}{2\pi}\ t_I(k_y)\{\mathrm{Tr}[g^{-+}_{RL}(x_0,k_y,\omega)]-\mathrm{Tr}[g^{-+}_{LR}(x_0,k_y,\omega)]\}. \tag{A4}$$

where the trace is taken over the Nambu space. In the presence of particle-hole symmetry, 11 and 22 components contribute equally. Therefore, the trace yields twice the contribution from the 11 component. For elastic tunneling processes (i.e., the interaction does not act across the tunneling matrix), one can use the Dyson equations[14]

$$g=g_0+g_0\ \hat{t}_I g=g_0+g\ \hat{t}_I g_0. \tag{A5}$$

Writing out the above equation for each component and note that in the bare level, $g_{0,RL}=0=g_{0,LR}$. We find

$$g^{-+}_{RL}=t_I(g^{--}_{RR}g^{-+}_{0,LL}-g^{-+}_{RR}g^{++}_{0,LL}), \tag{A6}$$

$$g^{-+}_{LR}=t_I(-g^{-+}_{0,LL}g^{++}_{RR}+g^{--}_{0,LL}g^{-+}_{RR}). \tag{A7}$$

By using $g^{++}+g^{--}=g^{-+}+g^{+-}$ and substituting Eqs. (A6) and (A7) into (A4), we obtain

$$I=2e\sum_{k_y}t_I^2\int_{-\infty}^{\infty}\frac{d\omega}{2\pi}\{g^{-+}_{0,LL,11}(\omega-eV)g^{+-}_{RR,11}(\omega)-g^{+-}_{0,LL,11}(\omega-eV)g^{-+}_{RR,11}(\omega)\}. \tag{A8}$$

Note that the frequency arguments of the bare Green's functions for the left electrode $g^{-+/+-}_{0,LL}$ has been shifted due to the applied bias eV between the two sides ($\mu_L-\mu_R=eV$). We emphasize that the Green's functions $g^{+-/-+}$ may contain contributions from interactions. $g^{+-/-+}$ can be expressed in terms of the bare ones $g_0^{+-/-+}$ and retarded/advanced Green's functions $g^{r,a}$ by the following equations:[14]

$$g^{+-/-+}(\omega)=[1+g^r(\omega)\ \hat{t}_I]g_0^{+-/-+}[\hat{t}_I g^a(\omega)+1]. \tag{A9}$$

One can further express $g^{r,a}$ in terms of the bare ones $g_0^{r,a}$ by virtue of the Dyson equations

$$g^{r,a}(\omega)=g_0^{r,a}(\omega)+g_0^{r,a}(\omega)\ \hat{t}_I g^{r,a}(\omega). \tag{A10}$$

Solving these equations, we obtain

$$g^{r,a}_{RR}(\omega)=\mathcal{T}^{r,a}_{RL}(\omega)g^{r,a}_{0,RR}(\omega), \tag{A11}$$

$$g^{r,a}_{LR}(\omega)=\mathcal{T}^{r,a}_{LR}(\omega)[t_I g^{r,a}_{0,LL}(\omega-eV)\tau_3 g^{r,a}_{0,RR}(\omega)], \tag{A12}$$

$$g^{r,a}_{RL}(\omega)=\mathcal{T}^{r,a}_{RL}(\omega)[t_I g^{r,a}_{0,RR}(\omega)\tau_3 g^{r,a}_{0,LL}(\omega-eV)], \tag{A13}$$

$$g^{r,a}_{LL}(\omega)=\mathcal{T}^{r,a}_{LR}(\omega)g^{r,a}_{0,LL}(\omega-eV), \tag{A14}$$

where the sum over tunneling processes of all orders is signified by the factors

$$\mathcal{T}^{r,a}_{RL}(\omega)=[1-t_I^2 g^{r,a}_{0,RR}(\omega)\tau_3 g^{r,a}_{0,LL}(\omega-eV)\tau_3]^{-1},$$

$$\mathcal{T}^{r,a}_{LR}(\omega)=[1-t_I^2 g^{r,a}_{0,LL}(\omega-eV)\tau_3 g^{r,a}_{0,RR}(\omega)\tau_3]^{-1}.$$

Note that frequencies of particles and holes are shifted in *opposite* ways in $g_{0,LL}$: $g_{0,LL,11}(\omega-eV)$ and $g_{0,LL,22}(\omega+eV)$. This is essential in giving rise to the Andreev contributions in the tunneling current.

Incorporating Eqs. (A11)–(A14) with (A9), one can thus obtain $g^{-+/+-}_{RR}$ and substitute back into Eq. (A8). Finally, by using the relations

$$g_0^{-+}(\omega)=2\pi i f(\omega)\hat{A}(\omega), \tag{A15}$$

$$g_0^{+-}(\omega)=-2\pi i[1-f(\omega)]\ \hat{A}(\omega), \tag{A16}$$

where $f(\omega)$ is the Fermi function and $\hat{A}(\omega)$ is the spectral weight matrix given by Eq. (27), we obtain the current expressions (23)–(26).

2. N-DDW junctions

We now derive the current expressions for N-DDW junctions. These will be also applicable to NG junctions. We shall also show that in this case Andreev-like processes do not contribute to the tunneling current. In the absence of external fields, spin degree of freedom merely introduces a factor of 2. Thus the spin indices σ will be omitted in the following.

We first define the Keldysh Green's functions similarly to Eq. (A3)

$$g_{\alpha\beta}^{-+}(x_i,t;x_j,t')=+i\langle c_\beta^\dagger(x_j,t')c_\alpha(x_i,t)\rangle, \tag{A17}$$

$$g_{\alpha\beta}^{+-}(x_i,t;x_j,t')=-i\langle c_\alpha(x_i,t)c_\beta^\dagger(x_j,t')\rangle. \tag{A18}$$

Here the subscripts α, $\beta=\{R,L\}$ are labels for the electrodes (not to be confused with the labels for sublattices in the text). In terms of the Keldysh Green's functions the tunneling current can be written

$$I(t)=+e\sum_{l,r,\sigma}[t_I g_{RL}^{-+}(r,l)-t_I^*\ g_{LR}^{-+}(l,r)]. \tag{A19}$$

Similar to the previous section, the renormalized Green's functions g_{RL} and g_{LR} can be expressed as combinations of $g_{0,LL}$ and g_{RR}. This results in the exact formula

$$I=e\sum_{k_y,\sigma}t_I^2\int_{-\infty}^{\infty}\frac{d\omega}{2\pi}\{g_{0,LL}^{-+}(\omega-eV)g_{RR}^{+-}(\omega) -g_{0,LL}^{+-}(\omega-eV)g_{RR}^{-+}(\omega)\}. \tag{A20}$$

Note that here, unlike the previous section, the tunneling matrix is $\hat{t}_I=t_I\sigma_3$, where σ_3 is the third Pauli matrix in the Keldysh space.

By applying Eq. (A9) and carrying out similar calculations as for ND junctions, we find

$$g_{RR}^{-+}=2\pi i[f(\omega)M_R(\omega)+f(\omega-eV)M_L(\omega)], \tag{A21}$$

$$g_{RR}^{+-}=-2\pi i[(1-f(\omega))M_R(\omega)+(1-f(\omega-eV))M_L(\omega)], \tag{A22}$$

with $M_R(\omega)=A_R(\omega)|1+t_I g_{RL}^r(\omega)|^2$ and $M_L(\omega)=t_I^2A_L(\omega-eV)|g_{RR}^r(\omega)|^2$. In the last expressions we have used $g_{RL}^r=(g_{LR}^a)^*$. Note that M_L contains the spectral weight A_L of the normal electrode. It is associated with tunneling processes where a particle is reflected back into the left side and at the same time a particle-hole pair is transmitted into the right; this is reminiscent of the Andreev channel in ND tunneling [see the integrand in Eq. (26)]. Substituting the above results into the current expression Eq. (A20), we obtain for the terms in the braces in the integrand

$$4\pi^2[f(\omega-eV)-f(\omega)]A_L(\omega-eV)M_R(\omega), \tag{A23}$$

which leads to the current expression (39).

*E-mail address: mou@phys.nthu.edu.tw

[1] I. Giaever, Phys. Rev. Lett. **5**, 147 (1960); **5**, 464 (1960).

[2] E. L. Wolf, *Principles of Electron Tunneling Spectroscopy* (Oxford University Press, New York, 1985).

[3] C-R Hu, Phys. Rev. Lett. **72**, 1526 (1994).

[4] G.E. Blonder, M. Tinkham, and T.M. Klapwijk, Phys. Rev. B **25**, 4515 (1982); S. Kashiwaya, Y. Tanaka, M. Koyanagi, H. Takashima, and K. Kajimura, *ibid.* **51**, 1350 (1995) for extension to the *d*-wave case.

[5] See, for example, Y. Tamura, Y. Tanaka, M. Ogata, and S. Kashiwaya, Phys. Rev. B **60**, 9817 (1999).

[6] M.P. Samanta and S. Datta, Phys. Rev. B **57**, 10 972 (1998).

[7] C. L. Wu, Ph.D. thesis, National Tsing Hua University, Hsinshu, Taiwan, 2000; C.L. Wu, C.-Y. Mou, and D. Chang, Phys. Rev. B **63**, 172503 (2001).

[8] J.C. Cuevas, A. Martín-Rodero, and A. Levy Yeyati, Phys. Rev. B **54**, 7366 (1996).

[9] The Green's function approach has also been applied at the quasiclassical level; see, for example, T. Luke, U. Eckern, and A. Shelankov, Phys. Rev. B **63**, 064510 (2001).

[10] C. Caroli, R. Combescot, P. Nozieres, and D. Saint-James, J. Phys. C **4**, 916 (1971).

[11] X.Z. Yan, H.W. Zhao, and C.R. Hu, Phys. Rev. B **61**, 14 759 (2000).

[12] The dimensionality of two is not essential; it is chosen here mainly for current experimental and theoretical interests. Our formulation is equally applicable to 3D cases.

[13] G. D. Mahan, *Many Particle Physics*, 2nd ed. (Plenum, New York, 1990), p. 788.

[14] L.V. Keldysh, Sov. Phys. JETP **20**, 1018 (1965).

[15] See, for example, J. D. Jackson, *Classical Electrodynamics*, 2nd ed. (Wiley, New York, 1975).

[16] S-T Wu and C.-Y. Mou, Phys. Rev. B **66**, 012512 (2002).

[17] Here, for simplicity, we have omitted the labels for electrodes $\{L,R\}$ [see Eq. (A1) in the Appendix].

[18] Y.S. Barush and A.A. Svidzinsky, Phys. Rev. B **55**, 15 282 (1997).

[19] M. Fogelström, D. Rainer, and J.A. Sauls, Phys. Rev. Lett. **79**, 281 (1997).

[20] P. G. de Gennes, *Superconductivity of Metals and Alloys* (Addison-Wesley, New York, 1989).

[21] M. Aprili, E. Badica, and L.H. Greene, Phys. Rev. Lett. **83**, 4630 (1999).

[22] Y. Dagan and G. Deutscher, Phys. Rev. Lett. **87**, 177004 (2001).

[23] W.P. Su, J.R. Schrieffer, and A.J. Heeger, Phys. Rev. Lett. **42**, 1698 (1979).

[24] In reality the bond length in polyacetylene alternates with a variation of about 6% in the single and the double bonds.

[25] See, for example, T. Timusk and B. Statt, Rep. Prog. Phys. **62**, 61 (1999), and references therein.
[26] S. Chakravarty, R.B. Laughlin, D.K. Morr, and C. Nayak, Phys. Rev. B **63**, 094503 (2001).
[27] C. Honerkamp and M. Sigrist, J. Phys.: Condens. Matter **13**, 11 669 (2001).
[28] M. Fujita, K. Wakabayashi, K. Nakada, and K. Kusakabe, J. Phys. Soc. Jpn. **65**, 1920 (1996).
[29] A. Levy Yeyati, A. Martín-Rodero, and F.J. García-Vidal, Phys. Rev. B **51**, 3743 (1995).